

A fully discrete stable discontinuous Galerkin method for the thin film epitaxy problem without slope selection [☆]



Yinhua Xia

School of Mathematical Sciences, University of Science and Technology of China, Hefei, Anhui 230026, PR China

ARTICLE INFO

Article history:

Received 16 June 2014
Received in revised form 19 September 2014
Accepted 21 September 2014
Available online 8 October 2014

Keywords:

Discontinuous Galerkin method
Thin film epitaxy problem
Convex splitting method
Unconditional energy stability
Spectral deferred correction method
Long time simulation

ABSTRACT

In this paper, we develop an energy stable fully discrete discontinuous Galerkin (DG) finite element method for the thin film epitaxy problem. Based on the method of lines, we construct and prove the energy stability of the spatial semi-discrete DG scheme firstly. To avoid the strict time step restriction of the explicit time integration method, the first order convex splitting method is used to get an unconditionally stable fully discrete DG method, which is a linearly implicit scheme for this nonlinear problem. The energy stability of the fully discrete convex splitting DG scheme is also proved. To improve the temporal accuracy, spectral deferred correction (SDC) method is adapted to achieve the high order accuracy in both time and space. Combining with the convex splitting method, the SDC method can be linearly solvable, high order accurate and stable in our numerical tests. These advantages ensure that the resulting fully discrete DG scheme is efficient to perform the long time simulation of the thin film epitaxy model. Numerical experiments of the accuracy and long time simulation show the capability and efficiency of the method.

© 2014 Elsevier Inc. All rights reserved.

1. Introduction

The epitaxial thin film model is the gradient flow with the energy

$$E(u) = \int_{\Omega} \left(F(\nabla u) + \frac{\epsilon^2}{2} |\Delta u|^2 \right) d\mathbf{x}, \quad (1.1)$$

where $\Omega \in \mathbf{R}^d$ with $d \geq 2$, $u : \Omega \rightarrow \mathbf{R}$ is the height function, $F(\nabla u)$ is a smooth function of its argument ∇u , and ϵ is a constant. This model arises in the phenomenological macroscopic coarsening processes, which usually take place on a very long time scale for large systems. The first part of the energy,

$$E^{ES}(u) = \int_{\Omega} F(\nabla u) d\mathbf{x},$$

[☆] Research supported by NSFC grant No. 11101400, No. 11371342, No. 11471306, Doctoral Fund of Ministry of Education of China No. 20113402120015 and SRF 2012940 for ROCS SEM.

E-mail address: yhxia@ustc.edu.cn.

represents the Ehrlich–Schwoebel energy, which is the higher energy barrier for the absorbed atoms to overcome and stick to a step from an upper terrace. The second part of the energy,

$$E^{SD}(u) = \int_{\Omega} \frac{\epsilon^2}{2} |\Delta u|^2 d\mathbf{x},$$

represents the surface diffusion effect. In [13], the so-called no-slope-selection Ehrlich–Schwoebel energy is defined by the integral of $F(\nabla u) = -\frac{1}{2} \ln(1 + |\nabla u|^2)$, in which the function $F(\nabla u)$ is unbounded below. The chemical potential is defined by the variational derivative of the energy, i.e.

$$\mu := \frac{\delta E(u)}{\delta u} = \nabla \cdot \left(\frac{\nabla u}{1 + |\nabla u|^2} \right) + \epsilon^2 \Delta^2 u. \quad (1.2)$$

Then the gradient flow follows,

$$\partial_t u = -\mu = -\nabla \cdot \left(\frac{\nabla u}{1 + |\nabla u|^2} \right) - \epsilon^2 \Delta^2 u, \quad (1.3)$$

with the Neumann boundary condition

$$\frac{\partial u}{\partial \mathbf{v}} = \frac{\partial \Delta u}{\partial \mathbf{v}} = 0, \quad \text{on } \partial\Omega, \quad (1.4)$$

or the periodic boundary condition, where \mathbf{v} is the unit normal vector on $\partial\Omega$ pointing exterior to Ω . Eq. (1.3) is called the no-slope-selection thin film model. Under the assumption that the slope $|\nabla u|$ is small, Eq. (1.3) can be approximated by

$$\partial_t u = -\nabla \cdot ((1 - |\nabla u|^2) \nabla u) - \epsilon^2 \Delta^2 u, \quad (1.5)$$

in which the Ehrlich–Schwoebel effect becomes $F(\nabla u) = \frac{1}{4} (|\nabla u|^2 - 1)^2$. This model has a slope selection mechanism, in which $|\nabla u| = 1$ is preferred. Eq. (1.5) is called the slope-selection thin film model.

Various unconditionally stable first order [20,2] and second order [19] temporal discretization schemes have been developed for the thin film model recently, based on the convex splitting technique derived in [10] for the Allen–Cahn and Cahn–Hilliard equations. In [23], the first, second and third order time accurate schemes also have been explored, where the energy stability for the first order scheme is based on the assumption of the numerical solution itself. For the spatial discretization, usually the central finite difference or the spectral method has been adopted for the periodic problems. In this paper, the discontinuous Galerkin (DG) method will be developed for the general boundary condition and domain problems. Another advantage of the discontinuous Galerkin method is the arbitrary high order accuracy by choosing the local approximating basis. Meanwhile, the spectral deferred correction (SDC) method [9,21] is used to achieve the high order accuracy for the temporal discretization.

The discontinuous Galerkin method is a class of finite element methods, in which using the discontinuous, piecewise polynomial basis as the solution and test spaces. It was first developed for solving the hyperbolic problems, which contains only first order spatial derivatives, e.g. Reed and Hill [18] for solving the linear time-independent neutron transport equation, and Cockburn et al. [4–7] for the nonlinear hyperbolic conservation laws. Then the DG method was generalized to the partial differential equations (PDEs) containing higher than the first order derivatives in several different approaches, e.g. interior penalty DG [1], local DG [24], direct DG [16], and DG based on multiple integration by parts [3] etc. The main idea in these different DG approaches is to choose the numerical fluxes carefully to ensure the energy stability, based on different weak forms of the problem. In this paper, we will use the framework of the local DG (LDG) method to develop the DG scheme for the thin film model. There are two steps in the LDG framework: first rewriting the problem into the form which contains only first order derivatives, and then applying the DG weak form by choosing the numerical fluxes to ensure energy stability. DG and LDG methods also have several attractive properties, such as arbitrary high order accuracy, the flexibility for arbitrary h and p adaptivity and their excellent parallel efficiency.

For PDEs containing higher order spatial derivatives, the explicit time discretization will suffer from the extremely small time step restriction for stability, but not for accuracy. It would therefore be desirable to use either nonlocal or implicit time discretization techniques to alleviate this problem, especially for the thin film model in which the long time simulation is needed for the coarsening process. Based on the idea of the convex splitting method for the Allen–Cahn and Cahn–Hilliard equations [10], the first and second order convex splitting methods for the thin-film model have been proposed in [2,20] and [19], respectively. In the convex splitting scheme, one first splits the energy into convex and concave parts. Then one discretizes the terms of the variational derivative implicitly for the convex part, and explicitly for the concave part of the energy respectively. The convex splitting method is unconditionally energy stable and uniquely solvable, regardless of the time step. Unfortunately, these schemes are only first or second order accurate, and not easy to extend to higher order accurate ones. In [21], some efficient semi-implicit time discretization methods have been explored coupled with LDG spatial discretization to obtain the uniformly high order fully discrete scheme, such as SDC method, exponential time differencing (ETD) method and additive Runge–Kutta (ARK) method. Coupled with the convex splitting method, we will construct a stable and linearly solvable SDC DG method for the thin film model, which is high order accurate in both space and time.

The organization of the paper is as follows. In Section 2, we will develop the local discontinuous Galerkin method for the thin film model and prove its discrete energy stability. In Section 3, we first present the first order, linear convex splitting method coupled with the LDG spatial discretization scheme, and prove that the fully-discrete scheme is unconditionally energy stable. Then, we introduce the linearly implicit SDC method coupled with the convex splitting DG scheme to achieve the uniform high order accuracy. Numerical experiments are presented in Section 4, testing the performance of the fully discrete high order scheme. Finally, we give the concluding remarks in Section 5.

2. Local discontinuous Galerkin method

In this section, we will develop the local discontinuous Galerkin (LDG) semi-discrete scheme for the no-slope-selection thin film model.

We consider a subdivision \mathcal{T}_h of Ω with shape-regular elements K , and denote the union of the boundary faces of elements $K \in \mathcal{T}_h$ by \mathcal{E}_h , i.e. $\mathcal{E}_h = \bigcup_{K \in \mathcal{T}_h} \partial K$, and $\Gamma_0 = \Gamma \setminus \partial\Omega$. We set

$$V_h := \{v \in L^2(\Omega) : v|_K \in P^k(K), \forall K \in \mathcal{T}_h\}, \quad (2.6)$$

$$\mathbf{W}_h := \{\mathbf{v} \in (L^2(\Omega))^d : \mathbf{v}|_K \in (P^k(K))^d, \forall K \in \mathcal{T}_h\}, \quad (2.7)$$

where $P^k(K)$ is the space of polynomial functions of degree at most k on K . Notice that functions in V_h and \mathbf{W}_h are allowed to be completely discontinuous across element interfaces. We denote all the interior faces by \mathcal{E}_h^i , that $e \in \mathcal{E}_h^i$ if there are two elements K_1 and K_2 in \mathcal{T}_h such that $e = \partial K_1 \cap \partial K_2$. And all the boundary faces are denoted by $\Gamma_h := \mathcal{E}_h \setminus \mathcal{E}_h^i$, that $e \in \Gamma_h$ if there is an element K in \mathcal{T}_h such that $e = \partial K \cap \partial\Omega$.

To develop the LDG scheme, we first rewrite Eq. (1.3) into the system form,

$$u_t = -\nabla \cdot \mathbf{S} - \epsilon^2 \nabla \cdot \mathbf{R}, \quad (2.8a)$$

$$\mathbf{P} = \nabla u, \quad (2.8b)$$

$$v = \nabla \cdot \mathbf{P}, \quad (2.8c)$$

$$\mathbf{R} = \nabla v, \quad (2.8d)$$

$$\mathbf{S} = \frac{\mathbf{P}}{1 + |\mathbf{P}|^2}, \quad (2.8e)$$

which contains only first order spatial derivatives. Next, we obtain the weak formulation of the exact solution. Multiplying the equations in the system (2.8) by the test functions ϕ , $\boldsymbol{\eta}$, φ , $\boldsymbol{\xi}$ and ζ , respectively, integrating on each elements K , and adding over all $K \in \mathcal{T}_h$, we get the weak formulation that is satisfied by the exact solution $(u, \mathbf{P}, v, \mathbf{R}, \mathbf{S})$:

$$(u_t, \phi)_h = -\langle \mathbf{S} \cdot \mathbf{v}, \phi \rangle_h + (\mathbf{S}, \nabla \phi)_h - \epsilon^2 \langle \mathbf{R} \cdot \mathbf{v}, \phi \rangle_h + \epsilon^2 (\mathbf{R}, \nabla \phi)_h, \quad (2.9a)$$

$$(\mathbf{P}, \boldsymbol{\eta})_h = \langle u, \boldsymbol{\eta} \cdot \mathbf{v} \rangle_h - (u, \nabla \cdot \boldsymbol{\eta})_h, \quad (2.9b)$$

$$(v, \varphi)_h = \langle \mathbf{P} \cdot \mathbf{v}, \varphi \rangle_h - (\mathbf{P}, \nabla \varphi)_h, \quad (2.9c)$$

$$(\mathbf{R}, \boldsymbol{\xi})_h = \langle v, \boldsymbol{\xi} \cdot \mathbf{v} \rangle_h - (v, \nabla \cdot \boldsymbol{\xi})_h, \quad (2.9d)$$

$$(\mathbf{S}, \zeta)_h = \left(\frac{\mathbf{P}}{1 + |\mathbf{P}|^2}, \zeta \right)_h, \quad (2.9e)$$

for all the test functions $(\phi, \varphi, \boldsymbol{\eta}, \boldsymbol{\xi}, \zeta)$. Here \mathbf{v} is the outward normal vector to ∂K . We have used the notation

$$(u, v)_h := \sum_{K \in \mathcal{T}_h} \int_K u(\mathbf{x})v(\mathbf{x})d\mathbf{x},$$

$$\langle u, v \rangle_h := \sum_{K \in \mathcal{T}_h} \int_{\partial K} u(\mathbf{x})v(\mathbf{x})ds,$$

$$(\boldsymbol{\eta}, \boldsymbol{\xi})_h := \sum_{K \in \mathcal{T}_h} \int_K \boldsymbol{\eta}(\mathbf{x}) \cdot \boldsymbol{\xi}(\mathbf{x})d\mathbf{x},$$

and the definition of L^2 norm on the domain Ω can be given by

$$\|u\|_{L^2} = \sqrt{(u, u)_h}.$$

Based on the weak formulation (2.9), the semi-discrete scheme of the thin film model given by the LDG method is defined by the spatial discretization of the system (2.9) in the space V_h, \mathbf{W}_h . To simplify the notation, we still use $u, v, \mathbf{P}, \mathbf{R}, \mathbf{S}$

as the numerical solution. The semi-discrete LDG scheme for Eq. (2.9) is defined as: Find $u, v \in V_h$ and $\mathbf{P}, \mathbf{R}, \mathbf{S} \in \mathbf{W}_h$, such that

$$(u_t, \phi)_h = -(\widehat{\mathbf{S}} \cdot \mathbf{v}, \phi)_h + (\mathbf{S}, \nabla \phi)_h - \epsilon^2 (\widehat{\mathbf{R}} \cdot \mathbf{v}, \phi)_h + \epsilon^2 (\mathbf{R}, \nabla \phi)_h, \tag{2.10a}$$

$$(\mathbf{P}, \boldsymbol{\eta})_h = (\widehat{u}, \boldsymbol{\eta} \cdot \mathbf{v})_h - (u, \nabla \cdot \boldsymbol{\eta})_h, \tag{2.10b}$$

$$(v, \varphi)_h = (\widehat{\mathbf{P}} \cdot \mathbf{v}, \varphi)_h - (\mathbf{P}, \nabla \varphi)_h, \tag{2.10c}$$

$$(\mathbf{R}, \boldsymbol{\xi})_h = (\widehat{v}, \boldsymbol{\xi} \cdot \mathbf{v})_h - (v, \nabla \cdot \boldsymbol{\xi})_h, \tag{2.10d}$$

$$(\mathbf{S}, \boldsymbol{\zeta})_h = \left(\frac{\mathbf{P}}{1 + |\mathbf{P}|^2}, \boldsymbol{\zeta} \right)_h, \tag{2.10e}$$

for all $\phi, \varphi \in V_h$ and $\boldsymbol{\eta}, \boldsymbol{\xi}, \boldsymbol{\zeta} \in \mathbf{W}_h$. Here $\widehat{\mathbf{S}}, \widehat{\mathbf{R}}, \widehat{u}, \widehat{\mathbf{P}}$ and \widehat{v} are the numerical traces (numerical fluxes). To complete the definition of the method, we need to define these numerical fluxes.

Now let e be an interior face shared by the elements K_L and K_R and define the outward unit normal vectors \mathbf{v}_L and \mathbf{v}_R on e respectively. For our purpose “left” and “right” can be uniquely defined for each face according to any fixed rule. For example, \mathbf{v}_0 can be chosen as a constant vector. The left element K_L to the face e requires that $\mathbf{v}_L \cdot \mathbf{v}_0 \leq 0$, and the right one K_R requires that $\mathbf{v}_R \cdot \mathbf{v}_0 > 0$. If w is a function on K_L and K_R , but possibly discontinuous across e , let w_L denote $(w|_{K_L})|_e$ and w_R denote $(w|_{K_R})|_e$, the left and right traces, respectively. The numerical fluxes are chosen based on the stability analysis. It turns out that the simple alternating numerical fluxes can guarantee the energy stability, such as

$$\widehat{\mathbf{S}} = \mathbf{S}_L, \quad \widehat{\mathbf{R}} = \mathbf{R}_L, \quad \widehat{u} = u_R, \quad \widehat{\mathbf{P}} = \mathbf{P}_L, \quad \widehat{v} = v_R. \tag{2.11}$$

For boundary faces with the Neumann boundary condition (1.4), the numerical fluxes will be chosen as

$$\widehat{\mathbf{S}} \cdot \mathbf{v} = 0, \quad \widehat{\mathbf{R}} \cdot \mathbf{v} = 0, \quad \widehat{u} = u_I, \quad \widehat{\mathbf{P}} \cdot \mathbf{v} = 0, \quad \widehat{v} = v_I, \tag{2.12}$$

where u_I and v_I mean the numerical traces from the inside of the computational domain. In the following proof of the energy stability, we can see that the choice of the alternating numerical fluxes is not unique and the crucial part is to take \widehat{u} and $\widehat{\mathbf{S}}, \widehat{\mathbf{R}}$ from opposite sides, also \widehat{v} and $\widehat{\mathbf{P}}$ from opposite sides. Besides the alternating fluxes, the central fluxes or the linear combination of the alternating fluxes also work for the stability analysis. However, similar to the LDG scheme for the heat equation $u_t = u_{xx}$ [8], non-alternating numerical fluxes could lead to the suboptimal convergence rate sometimes.

Obviously, the scheme is conservative, by choosing the test function $\phi = 1$ in the scheme (2.10). Next, we will prove the energy stability for semi-discrete LDG scheme (2.10) with the alternating numerical fluxes and the Neumann or periodic boundary condition.

Proposition 2.1 (Energy stability for the semi-discrete DG scheme). *The solution to the LDG scheme (2.10) with numerical fluxes (2.11) and the Neumann boundary condition (2.12) or the periodic boundary condition satisfies the energy stability*

$$\frac{d}{dt} E_h(\mathbf{P}, v) = \frac{d}{dt} \int_{\Omega} \left(F(\mathbf{P}) + \frac{\epsilon^2}{2} v^2 \right) d\mathbf{x} \leq 0, \tag{2.13}$$

where $F(\mathbf{P}) = -\frac{1}{2} \ln(1 + |\mathbf{P}|^2)$.

Proof. Taking the test function $\phi = u_t$ in Eq. (2.10a) of the LDG scheme (2.10), we have

$$(u_t, u_t)_h = -(\widehat{\mathbf{S}} \cdot \mathbf{v}, u_t)_h + (\mathbf{S}, \nabla u_t)_h - \epsilon^2 (\widehat{\mathbf{R}} \cdot \mathbf{v}, u_t)_h + \epsilon^2 (\mathbf{R}, \nabla u_t)_h. \tag{2.14}$$

After taking the time derivative of Eqs. (2.10b) and (2.10c) and choosing the test functions $\boldsymbol{\eta} = \mathbf{S}, \mathbf{R}$, and $\varphi = v$, we obtain

$$(\mathbf{P}_t, \mathbf{S})_h = (\widehat{u}_t, \mathbf{S} \cdot \mathbf{v})_h - (u_t, \nabla \cdot \mathbf{S})_h, \tag{2.15}$$

$$(\mathbf{P}_t, \mathbf{R})_h = (\widehat{u}_t, \mathbf{R} \cdot \mathbf{v})_h - (u_t, \nabla \cdot \mathbf{R})_h, \tag{2.16}$$

$$(v_t, v)_h = (\widehat{\mathbf{P}}_t \cdot \mathbf{v}, v)_h - (\mathbf{P}_t, \nabla v)_h. \tag{2.17}$$

Then we choose the test function $\boldsymbol{\xi} = \mathbf{P}_t$ and $\boldsymbol{\zeta} = \mathbf{P}_t$ in Eqs. (2.10d) and (2.10e) of the scheme and we get

$$(\mathbf{R}, \mathbf{P}_t)_h = (\widehat{v}, \mathbf{P}_t \cdot \mathbf{v})_h - (v, \nabla \cdot \mathbf{P}_t)_h, \tag{2.18}$$

$$(\mathbf{S}, \mathbf{P}_t)_h = \left(\frac{\mathbf{P}}{1 + |\mathbf{P}|^2}, \mathbf{P}_t \right)_h. \tag{2.19}$$

Now let (2.14) – (2.15) – ϵ^2 (2.16) + ϵ^2 (2.18) + ϵ^2 (2.17) + (2.19), and we find

$$\begin{aligned}
 (u_t, u_t)_h + \epsilon^2(v_t, v)_h &= \left(\frac{\mathbf{P}}{1 + |\mathbf{P}|^2}, \mathbf{P}_t \right)_h \\
 &\quad - \langle \widehat{\mathbf{S}} \cdot \mathbf{v}, u_t \rangle_h + (\mathbf{S}, \nabla u_t)_h - \langle \widehat{u}_t \mathbf{v}, \mathbf{S} \rangle_h + (u_t, \nabla \cdot \mathbf{S})_h \\
 &\quad + \epsilon^2(-\langle \widehat{\mathbf{R}} \cdot \mathbf{v}, u_t \rangle_h + (\mathbf{R}, \nabla u_t)_h - \langle \widehat{u}_t \mathbf{v}, \mathbf{R} \rangle_h + (u_t, \nabla \cdot \mathbf{R})_h) \\
 &\quad + \epsilon^2(\langle \widehat{\mathbf{P}}_t \cdot \mathbf{v}, v \rangle_h - (\mathbf{P}_t, \nabla v)_h + \langle \widehat{\mathbf{v}} \mathbf{P}_t \rangle_h - (v, \nabla \cdot \mathbf{P}_t)_h).
 \end{aligned}$$

For the alternating numerical fluxes (2.11) on interior faces and the Neumann boundary condition (2.12) or the periodic boundary condition (with the same alternating numerical fluxes as (2.11)) on boundary faces, it is easy to check that

$$\begin{aligned}
 -\langle \widehat{\mathbf{S}} \cdot \mathbf{v}, u_t \rangle_h + (\mathbf{S}, \nabla u_t)_h - \langle \widehat{u}_t \mathbf{v}, \mathbf{S} \rangle_h + (u_t, \nabla \cdot \mathbf{S})_h &= 0, \\
 -\langle \widehat{\mathbf{R}} \cdot \mathbf{v}, u_t \rangle_h + (\mathbf{R}, \nabla u_t)_h - \langle \widehat{u}_t \mathbf{v}, \mathbf{R} \rangle_h + (u_t, \nabla \cdot \mathbf{R})_h &= 0, \\
 \langle \widehat{\mathbf{P}}_t \cdot \mathbf{v}, v \rangle_h - (\mathbf{P}_t, \nabla v)_h + \langle \widehat{\mathbf{v}} \mathbf{P}_t \rangle_h - (v, \nabla \cdot \mathbf{P}_t)_h &= 0.
 \end{aligned}$$

Thus, we see that

$$\frac{d}{dt} E_h(\mathbf{P}, v) = -\left(\frac{\mathbf{P}}{1 + |\mathbf{P}|^2}, \mathbf{P}_t \right)_h + \epsilon^2(v_t, v)_h = -(u_t, u_t)_h \tag{2.20}$$

which means that the discrete energy decreases at the rate of $\|u_t\|_{L^2}^2$. □

Remark 2.1. From the energy stability for the LDG scheme, only the intermediate variable \mathbf{P} and v can be bounded. So we cannot derive the H^2 stability for the LDG scheme. Consequently, we cannot give the error estimate based only on the energy stability.

3. Time discretization

When ϵ is small, the coarsening process occurs on a very long time scale. And also, the explicit time integration methods lead to a very strict time step for stability, due to the high order spatial derivatives. Therefore, the time discretization method for the thin film model requires long time accuracy and stability.

3.1. Convex splitting method

We employ the convex splitting method for the time discretization coupled with the discontinuous Galerkin spatial discretization, to obtain a fully discrete stable DG scheme for the thin film model.

First, we split the discrete energy $E_h(\mathbf{P}, v)$ as $E_h(\mathbf{P}, v) = E_h^i(\mathbf{P}, v) - E_h^e(\mathbf{P}, v)$, where

$$E_h^i(\mathbf{P}, v) = \int_{\Omega} \frac{1}{2} |\mathbf{P}|^2 + \frac{\epsilon^2}{2} v^2 d\mathbf{x}, \quad E_h^e(\mathbf{P}, v) = \frac{1}{2} \int_{\Omega} |\mathbf{P}|^2 + \ln(1 + |\mathbf{P}|^2) d\mathbf{x}.$$

There are many different ways to split the energy. Here we follow the energy splitting approach suggested in [2]. This splitting approach can lead to a linearly semi-implicit time discretization method, which is uniquely solvable obviously and efficient comparing to the nonlinearly implicit method. The corresponding convex splitting DG scheme is given by: Find $u^{n+1} \in V_h$ and $\mathbf{P}^{n+1}, \mathbf{R}^{n+1}, \mathbf{S}^{n+1} \in \mathbf{W}_h$,

$$\begin{aligned}
 \left(\frac{u^{n+1} - u^n}{\Delta t}, \phi \right)_h &= -\langle \widehat{\mathbf{P}}^n \cdot \mathbf{v}, \phi \rangle_h + (\mathbf{P}^n, \nabla \phi)_h - \langle \widehat{\mathbf{S}}^n \cdot \mathbf{v}, \phi \rangle_h + (\mathbf{S}^n, \nabla \phi)_h \\
 &\quad + \langle \widehat{\mathbf{P}}^{n+1} \cdot \mathbf{v}, \phi \rangle_h - (\mathbf{P}^{n+1}, \nabla \phi)_h - \epsilon^2 \langle \widehat{\mathbf{R}}^{n+1} \cdot \mathbf{v}, \phi \rangle_h + \epsilon^2 (\mathbf{R}^{n+1}, \nabla \phi)_h,
 \end{aligned} \tag{3.21}$$

where u^n, u^{n+1} represents the numerical solution at time level t^n and t^{n+1} respectively, and the time step $\Delta t = t^{n+1} - t^n$. The time step Δt could be chosen adaptively at each time level.

It is easy to see that the fully-discrete scheme is also conservative. Next, we will prove the energy stability for the fully-discrete DG scheme (3.21) with the choice of the numerical fluxes in the previous section.

Proposition 3.1 (Energy stability for the fully discrete DG scheme). *The solution to the LDG scheme (3.21) with the numerical fluxes (2.11) and the Neumann boundary condition (2.12) or the periodic boundary condition satisfies the energy stability*

$$E_h(\mathbf{P}^{n+1}, v^{n+1}) - E_h(\mathbf{P}^n, v^n) \leq 0, \tag{3.22}$$

where $E_h(\mathbf{P}, v) = \int_{\Omega} (F(\mathbf{P}) + \frac{\epsilon^2}{2} v^2) d\mathbf{x}$ and $F(\mathbf{P}) = -\frac{1}{2} \ln(1 + |\mathbf{P}|^2)$.

Proof. Let $\mathcal{D}u$ denote $u^{n+1} - u^n$. The fully discrete DG scheme can be written as

$$\begin{aligned} \frac{1}{\Delta t}(\mathcal{D}u, \phi)_h &= \langle \mathcal{D}\widehat{\mathbf{P}} \cdot \mathbf{v}, \phi \rangle_h - (\mathcal{D}\mathbf{P}, \nabla\phi)_h - \langle \widehat{\mathbf{S}}^n \cdot \mathbf{v}, \phi \rangle_h + (\mathbf{S}^n, \nabla\phi)_h \\ &\quad - \epsilon^2 \langle \widehat{\mathbf{R}}^{n+1} \cdot \mathbf{v}, \phi \rangle_h + \epsilon^2 (\mathbf{R}^{n+1}, \nabla\phi)_h. \end{aligned} \tag{3.23}$$

Choosing the test function $\phi = \mathcal{D}u$, we have

$$\begin{aligned} \frac{1}{\Delta t}(\mathcal{D}u, \mathcal{D}u)_h &= \langle \mathcal{D}\widehat{\mathbf{P}} \cdot \mathbf{v}, \mathcal{D}u \rangle_h - (\mathcal{D}\mathbf{P}, \nabla\mathcal{D}u)_h - \langle \widehat{\mathbf{S}}^n \cdot \mathbf{v}, \mathcal{D}u \rangle_h + (\mathbf{S}^n, \nabla\mathcal{D}u)_h \\ &\quad - \epsilon^2 \langle \widehat{\mathbf{R}}^{n+1} \cdot \mathbf{v}, \mathcal{D}u \rangle_h + \epsilon^2 (\mathbf{R}^{n+1}, \nabla\mathcal{D}u)_h. \end{aligned} \tag{3.24}$$

For Eq. (2.10b) of the LDG scheme, subtracting the equation at time level t^n from the equation at time level t^{n+1} , we get

$$(\mathcal{D}\mathbf{P}, \boldsymbol{\eta})_h = \langle \mathcal{D}\widehat{\mathbf{u}}, \boldsymbol{\eta} \cdot \mathbf{v} \rangle_h - (\mathcal{D}u, \nabla \cdot \boldsymbol{\eta})_h,$$

where $\mathcal{D}\mathbf{P} = \mathbf{P}^{n+1} - \mathbf{P}^n$. Then taking the test function $\boldsymbol{\eta} = \mathcal{D}\mathbf{P}, \mathbf{S}^n, \mathbf{R}^{n+1}$ separately, we obtain

$$(\mathcal{D}\mathbf{P}, \mathcal{D}\mathbf{P})_h = \langle \mathcal{D}\widehat{\mathbf{u}}, \mathcal{D}\mathbf{P} \cdot \mathbf{v} \rangle_h - (\mathcal{D}u, \nabla \cdot \mathcal{D}\mathbf{P})_h, \tag{3.25}$$

$$(\mathcal{D}\mathbf{P}, \mathbf{S}^n)_h = \langle \mathcal{D}\widehat{\mathbf{u}}, \mathbf{S}^n \cdot \mathbf{v} \rangle_h - (\mathcal{D}u, \nabla \cdot \mathbf{S}^n)_h, \tag{3.26}$$

$$(\mathcal{D}\mathbf{P}, \mathbf{R}^{n+1})_h = \langle \mathcal{D}\widehat{\mathbf{u}}, \mathbf{R}^{n+1} \cdot \mathbf{v} \rangle_h - (\mathcal{D}u, \nabla \cdot \mathbf{R}^{n+1})_h. \tag{3.27}$$

For Eq. (2.10c), taking the difference between two time levels and choosing test function $\varphi = v^{n+1}$ give

$$(\mathcal{D}v, v^{n+1})_h = \langle \mathcal{D}\widehat{\mathbf{P}} \cdot \mathbf{v}, v^{n+1} \rangle_h - (\mathcal{D}\mathbf{P}, \nabla v^{n+1})_h. \tag{3.28}$$

For Eq. (2.10d), choosing the test function $\boldsymbol{\xi} = \mathcal{D}\mathbf{P}$ at time level t^{n+1} shows that

$$(\mathbf{R}^{n+1}, \mathcal{D}\mathbf{P})_h = \langle \widehat{v}^{n+1}, \mathcal{D}\mathbf{P} \cdot \mathbf{v} \rangle_h - (v^{n+1}, \nabla \cdot \mathcal{D}\mathbf{P})_h. \tag{3.29}$$

For Eq. (2.10e), choosing the test function $\boldsymbol{\zeta} = \mathcal{D}\mathbf{P}$ at time level t^n leads to

$$(\mathbf{S}^n, \mathcal{D}\mathbf{P})_h = \left(\frac{\mathbf{P}^n}{1 + |\mathbf{P}^n|^2}, \mathcal{D}\mathbf{P} \right)_h. \tag{3.30}$$

Let (3.24) + (3.25) - (3.26) + (3.30) - ϵ^2 (3.27) + ϵ^2 (3.29) + ϵ^2 (3.28), and after a careful calculation we obtain

$$\frac{1}{\Delta t}(\mathcal{D}u, \mathcal{D}u)_h + (\mathcal{D}\mathbf{P}, \mathcal{D}\mathbf{P})_h + \epsilon^2(\mathcal{D}v, v^{n+1})_h = \left(\frac{\mathbf{P}^n}{1 + |\mathbf{P}^n|^2}, \mathcal{D}\mathbf{P} \right)_h, \tag{3.31}$$

with the help of the alternating numerical fluxes (2.11) on interior faces and the Neumann boundary condition (2.12) or the periodic boundary condition (with the same alternating numerical fluxes as (2.11)) on boundary faces. Notice that

$$2(\mathcal{D}v, v^{n+1})_h = (v^{n+1}, v^{n+1})_h - (v^n, v^n)_h + (\mathcal{D}v, \mathcal{D}v)_h,$$

and set $\mathcal{D}E_h^{ES} = E_h^{ES}(\mathbf{P}^{n+1}) - E_h^{ES}(\mathbf{P}^n)$, where $E_h^{ES}(\mathbf{P}) = \int_{\Omega} (-\frac{1}{2} \ln(1 + |\mathbf{P}|^2)) d\mathbf{x}$. Eq. (3.31) can be rewritten as

$$\begin{aligned} \frac{1}{\Delta t}(\mathcal{D}u, \mathcal{D}u)_h + \mathcal{D}E_h^{ES} + \frac{\epsilon^2}{2}((v^{n+1}, v^{n+1})_h - (v^n, v^n)_h + (\mathcal{D}v, \mathcal{D}v)_h) \\ = -(\mathcal{D}\mathbf{P}, \mathcal{D}\mathbf{P})_h + \left(\frac{\mathbf{P}^n}{1 + |\mathbf{P}^n|^2}, \mathcal{D}\mathbf{P} \right)_h + \mathcal{D}E_h^{ES}, \end{aligned}$$

or,

$$\begin{aligned} \frac{1}{\Delta t}(\mathcal{D}u, \mathcal{D}u)_h + E_h(\mathbf{P}^{n+1}, v^{n+1}) - E_h(\mathbf{P}^n, v^n) + \frac{\epsilon^2}{2}(\mathcal{D}v, \mathcal{D}v)_h \\ = -(\mathcal{D}\mathbf{P}, \mathcal{D}\mathbf{P})_h + \left(\frac{\mathbf{P}^n}{1 + |\mathbf{P}^n|^2}, \mathcal{D}\mathbf{P} \right)_h + \mathcal{D}E_h^{ES}, \end{aligned} \tag{3.32}$$

where $E_h(\mathbf{P}, v) = E_h^{ES}(\mathbf{P}) + \frac{\epsilon^2}{2}(v, v)_h$. Provided that the right hand side is not bigger than zero, then we obtain the energy stability

$$E_h(\mathbf{P}^{n+1}, v^{n+1}) - E_h(\mathbf{P}^n, v^n) \leq -\frac{1}{\Delta t}(\mathcal{D}u, \mathcal{D}u)_h - \frac{\epsilon^2}{2}(\mathcal{D}v, \mathcal{D}v)_h \leq 0.$$

In fact, it has been proved in [2] that

$$\begin{aligned} \mathcal{D}E_h^{ES} &= \int_{\Omega} \left(-\frac{1}{2} \ln(1 + |\mathbf{P}^{n+1}|^2) + \frac{1}{2} \ln(1 + |\mathbf{P}^n|^2) \right) d\mathbf{x}, \\ &= \frac{1}{2} \int_{\Omega} \ln \left(1 + \frac{|\mathbf{P}^n|^2 - |\mathbf{P}^{n+1}|^2}{1 + |\mathbf{P}^{n+1}|^2} \right) d\mathbf{x}, \\ &\leq \frac{1}{2} \int_{\Omega} \frac{|\mathbf{P}^n|^2 - |\mathbf{P}^{n+1}|^2}{1 + |\mathbf{P}^{n+1}|^2} d\mathbf{x}, \end{aligned}$$

and

$$\begin{aligned} \left(\frac{\mathbf{P}^n}{1 + |\mathbf{P}^n|^2}, \mathcal{D}\mathbf{P} \right)_h + \mathcal{D}E_h^{ES} &\leq \int_{\Omega} \left(\frac{\mathbf{P}^n \cdot \mathcal{D}\mathbf{P}}{1 + |\mathbf{P}^n|^2} + \frac{1}{2} \frac{|\mathbf{P}^n|^2 - |\mathbf{P}^{n+1}|^2}{1 + |\mathbf{P}^{n+1}|^2} \right) d\mathbf{x}, \\ &\leq \int_{\Omega} (\mathcal{D}\mathbf{P} \cdot \mathcal{D}\mathbf{P}) d\mathbf{x}, \end{aligned}$$

which means that the right hand side of Eq. (3.32) is not bigger than zero and yields the energy stability (3.22) for the fully discrete DG scheme (3.21). □

However, the convex splitting DG scheme (3.21) is only first order accurate in time. To improve the temporal accuracy, the spectral deferred correction (SDC) method will be employed, which was developed in [9] and adapted to the LDG method in [21].

3.2. Spectral deferred correction method with convex splitting

The SDC method is driven iteratively by the chosen low order method, for example the convex splitting method (3.21) here. An advantage of this method is that it is a one step method and can be constructed easily and systematically for any order of accuracy.

For convenience, we rewrite the convex splitting scheme (3.21) as

$$u^{n+1} = u^n + \Delta t(L(u^{n+1}) + N(u^n)), \tag{3.33}$$

where $L(u)$ represents the linearly implicit part and $N(u)$ represents the nonlinearly explicit part of the scheme, i.e.

$$L(u) = \Delta u - \epsilon^2 \Delta^2 u, \quad N(u) = -\Delta u - \nabla \cdot \left(\frac{\nabla u}{1 + |\nabla u|^2} \right).$$

The SDC method is a one step, multi-stage method. We divide the time interval $[t^n, t^{n+1}]$ into P subintervals by choosing the points $t_{n,m}$ for $m = 0, 1, \dots, P$ such that $t^n = t^{n,0} < t^{n,1} < \dots < t^{n,m} < \dots < t^{n,P} = t^{n+1}$. Let $\Delta t^{n,m} = t^{n,m+1} - t^{n,m}$ and $u_k^{n,m}$ denotes the k th order approximation to $u(t_{n,m})$. To avoid the instability of approximation at equispaced nodes for high order accuracy, the points $\{t^{n,m}\}_{m=0}^P$ are chosen to be the Chebyshev Gauss–Lobatto nodes on $[t^n, t^{n+1}]$. We can also use the Legendre Gauss–Lobatto nodes, or Chebyshev or Legendre Gauss–Radau or Gauss nodes. Starting from u^n , we give the algorithm to calculate u^{n+1} in the following.

1. Compute the initial approximation Use the convex splitting DG scheme (3.33) to compute a first order accurate approximate solution u_1 at the nodes $\{t_{n,m}\}_{m=1}^P$.

1.0. $u_1^{n,0} = u^n$.

1.1. For $m = 0, \dots, P - 1$

$$u_1^{n,m+1} = u_1^{n,m} + \Delta t^{n,m}(L(u_1^{n,m+1}) + N(u_1^{n,m})). \tag{3.34}$$

2. Compute successive corrections

2.0. For $k = 1, \dots, K$

$$u_{k+1}^{n,0} = u^n.$$

2.1. For $m = 0, \dots, P - 1$

$$u_{k+1}^{n,m+1} = u_{k+1}^{n,m} + \Delta t^{n,m}(L(u_{k+1}^{n,m+1}) - L(u_k^{n,m+1})) + I_m^{m+1}(L(u_k) + N(u_k)), \tag{3.35}$$

where $I_m^{m+1}(L(u_k) + N(u_k))$ is the integral of the P -th degree interpolating polynomial on the $P + 1$ points $(t^{n,m}, (L(u_k^{n,m}) + N(u_k^{n,m})))_{m=0}^P$ over the subinterval $[t^{n,m}, t^{n,m+1}]$, which is the numerical quadrature approximation of

$$\int_{t^{n,m}}^{t^{n,m+1}} L(u(\tau)) + N(u(\tau))d\tau. \tag{3.36}$$

Finally we have $u^{n+1} = u_{K+1}^{n,P}$.

It has been shown in [9,21] that the term $\Delta t^{n,m}(L(u_{k+1}^{n,m+1}) - L(u_k^{n,m+1}))$ in the SDC scheme (3.35) is helpful to the stability of the scheme, which is implicit and linear. The term $I_m^{m+1}(L(u_k) + N(u_k))$ in the scheme (3.35) is explicit and responsible for the accuracy increasing. Thus, the SDC scheme driven by the linearly implicit convex splitting scheme (3.21) is also linearly implicit, which is much easier than the nonlinearly implicit time discretization methods. We denote the SDC method (3.35) by SDC_K^P . The SDC_K^P has $\min(K + 1, P + 2)$ accuracy in time for $P > 1$ or $\min(K + 1, P + 1)$ accuracy for $P = 1$ when we choose the Gauss–Lobatto subinterval points [21].

Remark 3.1. According to the approach described in [21], $L(u)$ and $N(u)$ can also be chosen to be the linear part and nonlinear part of the equation, i.e.

$$L(u) = -\epsilon^2 \Delta^2 u, \quad N(u) = -\nabla \cdot \left(\frac{\nabla u}{1 + |\nabla u|^2} \right).$$

But the time step restriction for this approach is about $\Delta t \sim \mathcal{O}(\Delta x^2)$. From the numerical experiments in the next section, it can be found that the SDC method coupled with the unconditionally stable convex splitting method can maintain the stability numerically.

Remark 3.2. The residue equation for the SDC scheme (3.35) is

$$\sigma_k(t) = u^n + \int_{t^n}^t (L(u_k) + N(u_k))dt - u_k(t),$$

and the discretization of the residue equation is

$$\sigma_k^{n,m}(t) = u^n + I_0^m(L(u_k) + N(u_k)) - u_k^{n,m}.$$

The error equation is

$$\delta(t) = \int_{t^n}^t L(u_k + \delta) + N(u_k + \delta) - (L(u_k) + N(u_k))dt + \sigma_k(t),$$

and the discretization of the error equation is

$$\begin{aligned} \delta_k^{n,m+1} &= \delta_k^{n,m} + \Delta t^{n,m}(L(u_k^{n,m+1} + \delta_k^{n,m+1}) - L(u_k^{n,m+1})) + \Delta t^{n,m}(N(u_k^{n,m} + \delta_k^{n,m}) - N(u_k^{n,m})) \\ &\quad + \sigma_k^{n,m+1}(u^k) - \sigma_k^{n,m}(u^k). \end{aligned}$$

Hence, the SDC scheme is

$$\begin{aligned} u_{k+1}^{n,m+1} &= u_{k+1}^{n,m} + \Delta t^{n,m}(L(u_{k+1}^{n,m+1}) - L(u_k^{n,m+1})) + \Delta t^{n,m}(N(u_{k+1}^{n,m}) - N(u_k^{n,m})) \\ &\quad + I_m^{m+1}(L(u_k) + N(u_k)). \end{aligned}$$

The terms $\Delta t^{n,m}(L(u_{k+1}^{n,m+1}) - L(u_k^{n,m+1}))$ and $\Delta t^{n,m}(N(u_{k+1}^{n,m}) - N(u_k^{n,m}))$ in the SDC scheme is on the local truncation error level $\mathcal{O}(\Delta t^{k+2})$ and does not affect the accuracy of the scheme. Usually $L(u)$ is stiffer than $N(u)$, since $L(u)$ contains the fourth order derivative and $N(u)$ contains at most the second order derivative. But when ϵ is very small, $N(u)$ could be stiffer than $L(u)$ for not very small spatial step size h . Therefore, we omit the second term $\Delta t^{n,m}(N(u_{k+1}^{n,m}) - N(u_k^{n,m}))$ in case that $N(u)$ is stiffer than $L(u)$ for small ϵ .

4. Numerical experiments

In this section we present some numerical results for the no-slope-selection thin film model. Specifically, we use the DG spatial discretization coupled with the convex splitting temporal discretization or SDC method described in the previous sections. Each time step we solve the linear algebraic equations by the conjugate gradient method, due to only linear

Table 4.1

Temporal accuracy test in Example 4.1: L^1 and L^∞ errors and orders of $e_{\Delta t} = u_{h,\Delta t} - u_{h,2\Delta t}$ at $T = 0.32$. Here we choose $h = L_x/N = L_y/N$ with $N = 120$ and the piecewise P^k polynomial basis with $k = 4$. The refinement path is taken to be $\Delta t = \Delta t_0/2^m$, $m = 0, 1, 2, \dots$ and $\Delta t_0 = 0.2 * h$.

	m	$\ e_{\Delta t}\ _{L^1}$	Order	$\ e_{\Delta t}\ _{L^\infty}$	Order
SDC_1^0	0	1.26E-02	–	5.85E-02	–
	1	6.14E-03	1.03	2.88E-02	1.02
	2	3.20E-03	0.94	1.49E-02	0.95
	3	1.63E-03	0.97	7.53E-03	0.98
	4	8.22E-04	0.99	3.79E-03	0.99
SDC_1^1	0	4.10E-03	–	1.91E-02	–
	1	1.29E-03	1.67	6.00E-03	1.67
	2	3.70E-04	1.80	1.73E-03	1.80
	3	1.00E-04	1.89	4.70E-04	1.88
	4	2.62E-05	1.93	1.23E-04	1.93
SDC_2^2	0	4.34E-04	–	2.08E-03	–
	1	6.12E-05	2.61	3.12E-04	2.56
	2	9.31E-06	2.72	4.67E-05	2.69
	3	1.35E-06	2.79	6.76E-06	2.79
	4	1.89E-07	2.84	9.25E-07	2.87

even spatial derivatives in the implicit part of the scheme (3.33) and (3.35). For more complicated linear and nonlinear problems, we refer to the linear and nonlinear multigrid solver recently developed in [11,12] for the Cahn–Hilliard and Cahn–Hilliard–Hele–Shaw problems. We first present the accuracy tests that give the expected convergence rate of the scheme and the stability test of the scheme. Next, we will show the long time simulation of the scheme of the coarsening process, and the coarsening rate for the problem.

Example 4.1 (Accuracy and stability tests). Consider Eq. (1.3) in the two-dimensional domain $\Omega = [0, L_x] \times [0, L_y]$, with the periodic boundary condition. The initial condition is given by

$$u(x, y, 0) = 0.1 \sin^2\left(\frac{2\pi x}{L_x}\right) \sin\left(\frac{4\pi(y - 1.4)}{L_y}\right) - 0.1 \cos\left(\frac{2\pi(x - 2.0)}{L_x}\right) \sin\left(\frac{2\pi y}{L_y}\right).$$

Choose the parameters $\epsilon = 0.1$, and $L_x = L_y = 3.2$. This example is taken from [19] for easily comparison. We test the temporal and spatial accuracy at the final time $T = 0.32$ in the following ways. We choose the uniform mesh with the cell size $h = L_x/N = L_y/N$ and piecewise P^k polynomial basis in the approximation spaces V_h and W_h . To test the temporal accuracy numerically, we set the parameters $N = 120$ and $k = 4$ in the DG discretization fixed to ensure that the spatial discretization error is small enough, such that the temporal discretization error is dominant in the numerical experiment. Without the exact solution in this example, the numerical error is measured by

$$e_{\Delta t} = u_{h,\Delta t} - u_{h,2\Delta t},$$

where $u_{h,\Delta t}$ denotes the numerical solution under the spatial cell size h and temporal step size Δt . Table 4.1 shows the temporal accuracy and order in L^1 and L^∞ norms. We find that the SDC method (3.35) based on the first order convex splitting method (3.21) gives the expected convergence rate. To test the spatial accuracy numerically, the SDC_4^3 method is used for the temporal discretization to ensure that the spatial discretization error is dominant in our numerical experiment. The spatial error is measured by

$$e_h = u_r - u_{h,\Delta t},$$

where u_r is a reference numerical solution computed very accurately, with the temporal discretization SDC_4^3 and the spatial discretization piecewise P^4 polynomial on the mesh $N = 320$. Table 4.2 gives the spatial accuracy and order in L^1 and L^∞ norms. It shows that the DG discretization has the optimal convergence rate numerically.

Next, we will test the stability of the SDC scheme coupled with the DG discretization. We set the final time $T = 3.2$. In Table 4.3, it shows the L^1 and L^∞ norms of the error $e_{\Delta t} = u_r - u_{h,\Delta t}$ at $T = 3.2$ and the orders with the increasing time steps of $\Delta t = \Delta t_0/2^m$, $m = 0, -1, -2, -3$ and $\Delta t_0 = 0.2 * h$. Similar to the first accuracy test, we choose the parameters $N = 120$ and $k = 4$ in the DG discretization to ensure the temporal error is dominant in the test. Since the convergence is an asymptotic behavior, the convergence rate decreases when the time step becomes coarse. We find that the SDC scheme driven by the convex splitting method is always stable in the test. These numerical experiments verify that the fully discrete SDC DG method is stable and accurate for the thin film model.

Example 4.2 (Long time simulation). In this example, we will show the long time characteristics of the no-slope-selection model on the square domain with the random initial data. The square domain size is $L_x = L_y = 12.8$. The computational parameters are the spatial discretization cell size $h = L_x/N = L_y/N$ with $N = 120$ and the piecewise P^k polynomial basis

Table 4.2

Spatial accuracy test in Example 4.1: L^1 and L^∞ errors and orders of $e_h = u_r - u_{h,\Delta t}$ at $T = 0.32$. Here we choose time integration method SDC_k^p with $P = 3$ and $K = 4$, and the time step $\Delta t = 0.2 * h$ with $h = L_x/N = L_y/N$.

	N	$\ e_h\ _{L^1}$	Order	$\ e_h\ _{L^\infty}$	Order
p^0	20	8.77E-03	–	4.12E-02	–
	40	4.71E-03	0.90	2.20E-02	0.90
	80	2.42E-03	0.96	1.12E-02	0.97
	160	1.23E-03	0.98	5.66E-03	0.99
	320	6.17E-04	0.99	2.84E-03	1.00
p^1	20	2.58E-03	–	1.20E-02	–
	40	7.76E-04	1.73	3.61E-03	1.73
	80	2.17E-04	1.85	1.01E-03	1.84
	160	5.77E-05	1.91	2.71E-04	1.91
	320	1.50E-05	1.95	7.03E-05	1.95
p^2	20	5.63E-04	–	2.72E-03	–
	40	6.64E-05	3.08	3.48E-04	2.97
	80	7.25E-06	3.20	3.98E-05	3.13
	160	7.66E-07	3.24	4.11E-06	3.27
	320	7.80E-08	3.30	4.22E-07	3.28

Table 4.3

Stability test in Example 4.1: L^1 and L^∞ errors and orders of $e_{\Delta t} = u_r - u_{h,\Delta t}$ at $T = 3.2$. Here we choose $h = L_x/N = L_y/N$ with $N = 120$ and the piecewise P^k polynomial basis with $k = 4$. The refinement path is taken to be $\Delta t = \Delta t_0/2^m$, $m = 0, -1, -2, -3$ and $\Delta t_0 = 0.2 * h$.

	m	$\ e_{\Delta t}\ _{L^1}$	Order	$\ e_{\Delta t}\ _{L^\infty}$	Order
SDC_1^1	0	7.37E-03	–	2.14E-02	–
	-1	3.21E-02	2.14	8.22E-03	1.94
	-2	7.56E-02	1.24	2.03E-01	1.31
	-3	9.49E-02	0.33	2.97E-01	0.55
SDC_2^2	0	4.44E-04	–	1.41E-03	–
	-1	2.71E-03	2.61	8.35E-03	2.57
	-2	1.80E-02	2.73	4.82E-02	2.53
	-3	7.62E-02	2.08	1.89E-01	1.91

with $k = 2$; and the temporal discretization SDC_2^2 method with the time step $\Delta t = 0.2h$. In all three cases with different parameter $\epsilon = 0.02, 0.04$ and 0.08 , the initial conditions are the same, i.e. the random perturbation around 0.6 with a fluctuation no larger than 0.05. The periodic boundary condition is taken. Numerical convergence has been confirmed by the mesh refinement technique up to time $T = 400$. All three cases have been run till the system saturates, i.e. achieves the steady state.

In Fig. 4.1, the numerical results of u_h before saturation are showed at different time $T = 400, 2000$ and 10000 for the parameter $\epsilon = 0.02, 0.04$ and 0.08 . We can see that the coarsening speed is dependent on the parameter ϵ : the bigger the parameter ϵ , the faster the coarsening speed. In Fig. 4.2, the numerical saturation solutions are showed for three cases with different ϵ . We find that the saturation time also depends on the parameter ϵ : the bigger the parameter ϵ , the less saturation time. And, the saturation solutions in three cases share the similar pattern, i.e. almost the same hill (red region) and valley (blue region) size. Also, the height of the hill and the depth of the valley are almost the same in the same test case with the same ϵ . But the height of the mounds (hills and valleys), called $\eta(\epsilon)$, is different in different cases with different ϵ . We point out that our calculation here yields

$$\frac{\eta(0.02)}{\eta(0.04)} \approx \frac{\eta(0.04)}{\eta(0.08)} \approx 2,$$

which means the linear dependence of η on $1/\epsilon$, i.e. $\eta \sim \mathcal{O}(1/\epsilon)$.

The energy decay rate and surface roughness growth rate are of interest of to physicists and engineers. The discrete energy is defined in (2.13), and the roughness is

$$R(t) = \sqrt{\frac{1}{|\Omega|} \int_{\Omega} |u(\mathbf{x}, t) - \bar{u}(t)|^2 d\mathbf{x}}, \tag{4.37}$$

where $\bar{u} = \frac{1}{|\Omega|} \int_{\Omega} u(\mathbf{x}, t) d\mathbf{x}$. For the no-slope-selection model, the growth rates are predicted as $E(t) \sim \mathcal{O}(-\ln(t))$, $R(t) \sim \mathcal{O}(t^{-\frac{1}{2}})$ in [14,15]. Also the lower bound of the energy is

$$E(u) \geq \frac{L^2}{2} (\ln(\alpha) - \alpha + 1) := \gamma, \tag{4.38}$$

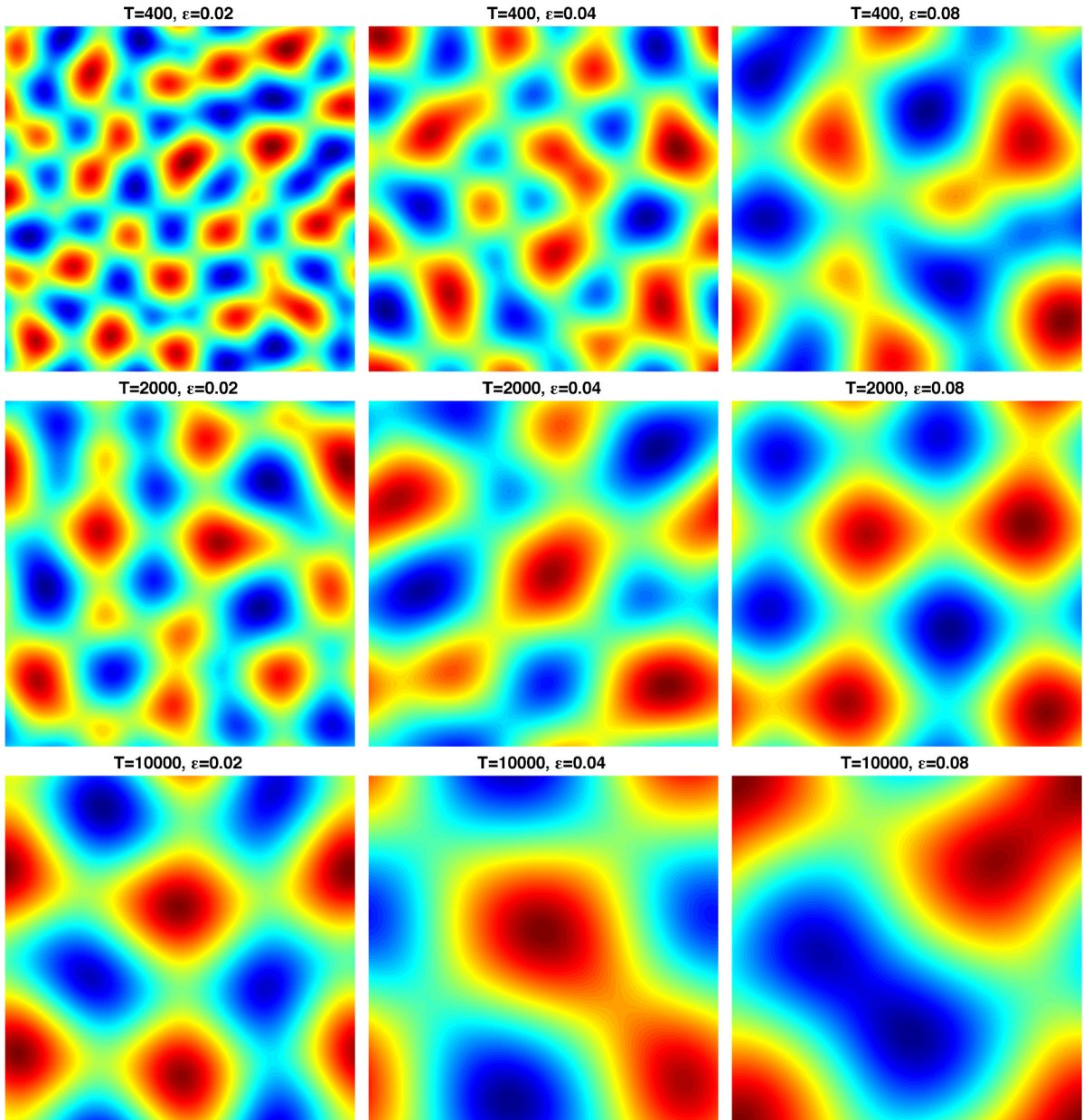


Fig. 4.1. Numerical results of height function u at indicated times before saturation for the different parameter ϵ . From the top to the bottom row, it corresponds to numerical solutions at the time $T = 400, 2000$ and 10000 . From the left to the right column, it corresponds to the numerical solutions for the parameter $\epsilon = 0.02, 0.04$ and 0.08 . The color scale changes with time. The hills (red) at early times are not as high as time at later times, and similarly with the valleys (blue). (For interpretation of the references to color in this figure legend, the reader is referred to the web version of this article.)

where $\alpha = (\frac{2\epsilon\pi}{T})^2$ [2]. This lower bound of the energy indicates that the decreasing rate of the energy will only hold when the system is away from the saturation. Similar to the height of the mounds (hills and valleys) $\eta(\epsilon)$, in Fig. 4.1 the minimum of the roughness $R_{\min}(\epsilon)$ yields

$$\frac{R_{\min}(0.02)}{R_{\min}(0.04)} \approx \frac{R_{\min}(0.04)}{R_{\min}(0.08)} \approx 2,$$

which is also linear dependent on $1/\epsilon$.

In Fig. 4.3, the decay rate of the energy has been shown for three cases $\epsilon = 0.02, 0.04$ and 0.08 respectively in the semi-log plots. In which, the blue lines represent the energy plot obtained by the simulations, the red lines are obtained by the least square linear fitting of the energy data till time $T = 400$ with $a_\epsilon + b_\epsilon \ln(t)$, and the black lines are the lower bound of the energy predicted in the formula (4.38). We can see that the energy decay rate satisfies an approximate $\ln(t)$

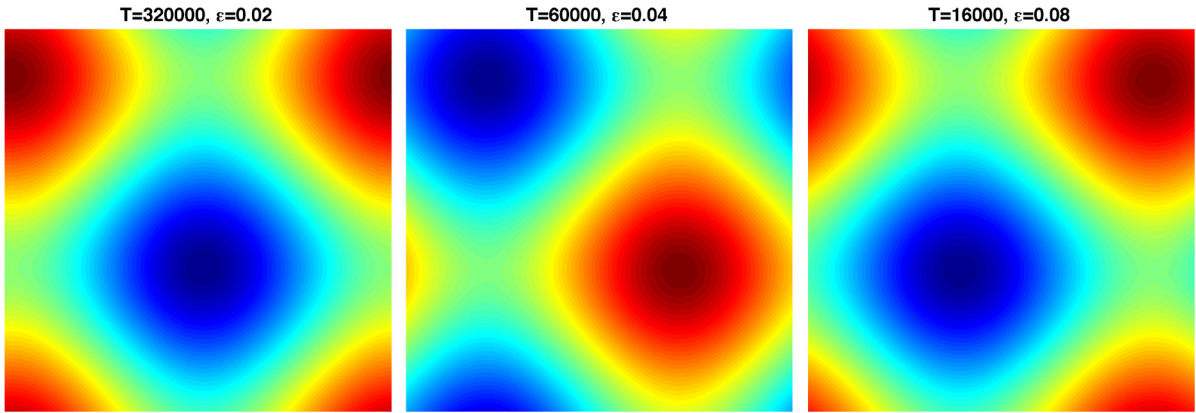


Fig. 4.2. Numerical results of height function u when the system saturates at indicated times for the parameter $\epsilon = 0.02, 0.04$ and 0.08 , from the most left to the right.

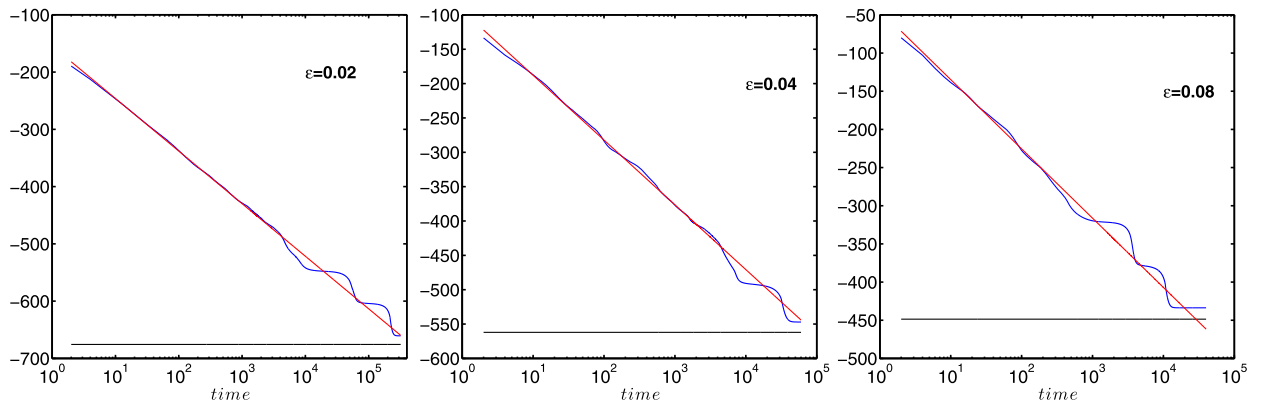


Fig. 4.3. Semi-log plots of the temporal evolution of the energy $E(t)$ for the parameter $\epsilon = 0.02, 0.04$ and 0.08 , from the most left to the right. The blue lines represent the energy plot obtained by the simulations, while the red lines are obtained by least squares approximations to the energy data. The black lines are the lower bound of the energy predicted in the formula (4.38).

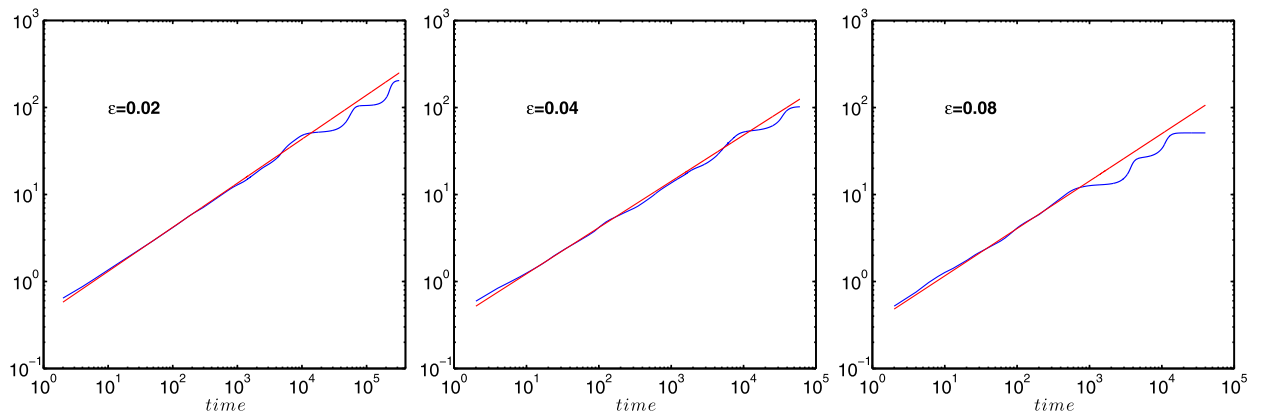


Fig. 4.4. Log-log plots of the temporal evolution of the roughness $R(t)$ for the parameter $\epsilon = 0.02, 0.04$ and 0.08 , from the most left to the right. The blue lines represent the roughness plot obtained by the simulations, while the red lines are obtained by least square approximations to the roughness data.

law for each case, and the lowest energy meets the predicted lower bound within 3.5% deviation. In Fig. 4.4, the decay rate of the roughness has been shown for three cases respectively in the log-log plots. In which, the blue lines represent the roughness plots obtained by the simulations, while the red lines are obtained by the least square linear approximation to the roughness data till time $T = 400$ with $a_r t^{b_r}$. In all three cases, b_r meets $1/2$ approximately within 5% deviation, which indicates the roughness decay rate is approximately $\mathcal{O}(t^{-1/2})$. From Figs. 4.3 and 4.4, we can also see the decay rates of the energy and roughness change dramatically when the mound size is close to the saturated mound size.

This long time simulation example shows the capability of the fully-discrete DG scheme. The SDC scheme coupled with the unconditionally stable convex splitting scheme is well suited to the thin film epitaxy model without slope selection. The stability property of the scheme is important in developing the numerical scheme for these type of calculations. Even though we did not give the simulation on the irregular and complex domain, naturally the DG scheme is capable of dealing with these situations.

5. Concluding remarks

We developed the discontinuous Galerkin method for the thin film epitaxy model without slope selection and proved the energy stability for the semi-discrete and fully-discrete schemes. The convex splitting temporal discretization method was adopted to get the fully-discrete scheme, which is proved to be unconditionally stable and linearly implicit. But the convex splitting method is only first order accurate in time. To achieve higher order temporal accuracy, the spectral deferred correction method was employed by combining with the low order unconditionally stable convex splitting method. Numerically we showed the stability and high order accuracy of the resulting fully-discrete DG scheme, in both time and space. Also, the long time simulations showed the capacity and efficiency of the scheme. The technique presented in this paper, combining the low order unconditionally stable scheme with the high order SDC method, can be easily generalized to the other gradient flow problems, e.g. Cahn–Hilliard type equation [22,17] and phase field crystal type equations. The resulting fully-discrete DG scheme can be stable, high order accurate and easy to handle the complicated domain and boundary conditions.

References

- [1] D.N. Arnold, F. Brezzi, B. Cockburn, L.D. Marini, Unified analysis of discontinuous Galerkin methods for elliptic problems, *SIAM J. Numer. Anal.* 39 (2001) 1749–1779.
- [2] W.B. Chen, S. Conde, C. Wang, X. Wang, S. Wise, A linear energy stable numerical scheme for epitaxial thin film growth model without slope selection, *J. Sci. Comput.* 52 (2012) 546–562.
- [3] Y. Cheng, C.-W. Shu, A discontinuous Galerkin finite element method for time dependent partial differential equations with higher order derivatives, *Math. Comput.* v77 (2008) 699–730.
- [4] B. Cockburn, S. Hou, C.-W. Shu, The Runge–Kutta local projection discontinuous Galerkin finite element method for conservation laws IV: the multidimensional case, *Math. Comput.* 54 (1990) 545–581.
- [5] B. Cockburn, S.-Y. Lin, C.-W. Shu, TVB Runge–Kutta local projection discontinuous Galerkin finite element method for conservation laws III: one dimensional systems, *J. Comput. Phys.* 84 (1989) 90–113.
- [6] B. Cockburn, C.-W. Shu, TVB Runge–Kutta local projection discontinuous Galerkin finite element method for conservation laws II: general framework, *Math. Comput.* 52 (1989) 411–435.
- [7] B. Cockburn, C.-W. Shu, The Runge–Kutta discontinuous Galerkin method for conservation laws V: multidimensional systems, *J. Comput. Phys.* 141 (1998) 199–224.
- [8] B. Cockburn, C.-W. Shu, The local discontinuous Galerkin method for time-dependent convection-diffusion systems, *SIAM J. Numer. Anal.* 35 (1998) 2440–2463.
- [9] A. Dutt, L. Greengard, V. Rokhlin, Spectral deferred correction methods for ordinary differential equations, *BIT Numer. Math.* 40 (2000) 241–266.
- [10] D.J. Eyre, Unconditionally gradient stable time marching the Cahn–Hilliard equation, in: J.W. Bullard, R. Kalia, M. Stoneham, L.Q. Chen (Eds.), *Computational and Mathematical Models of Microstructural Evolution*, vol. 53, Materials Research Society, Warrendale, 1998, pp. 1686–1712.
- [11] R. Guo, Y. Xu, Efficient solvers of discontinuous Galerkin discretization for the Cahn–Hilliard equations, *J. Sci. Comput.* 58 (2014) 380–408.
- [12] R. Guo, Y. Xia, Y. Xu, An efficient fully-discrete local discontinuous Galerkin method for the Cahn–Hilliard–Hele–Shaw system, *J. Comput. Phys.* 264 (2014) 23–40.
- [13] M.D. Johnson, C. Orme, A.W. Hunt, D. Graff, J. Sudijono, L.M. Sander, B.G. Orr, Stable and unstable growth in molecular beam epitaxy, *Phys. Rev. Lett.* 72 (1994) 116–119.
- [14] B. Li, J.-G. Liu, Thin film epitaxy with or without slope selection, *Eur. J. Appl. Math.* 14 (2003) 713–743.
- [15] B. Li, J.-G. Liu, Epitaxial growth without slope selection: energetics, coarsening, and dynamic scaling, *J. Nonlinear Sci.* 14 (2004) 429–451.
- [16] H. Liu, J. Yan, The Direct Discontinuous Galerkin (DDG) Methods for Diffusion Problems, *SIAM J. Numer. Anal.* 47 (2009) 675–698.
- [17] F. Liu, J. Shen, Stabilized semi-implicit spectral deferred correction methods for Allen–Cahn and Cahn–Hilliard equations, *Math. Methods Appl. Sci.* (2014), in press.
- [18] W.H. Reed, T.R. Hill, Triangular mesh method for the neutron transport equation, Technical report LA-UR-73-479, Los Alamos Scientific Laboratory, Los Alamos, NM, 1973.
- [19] J. Shen, C. Wang, X. Wang, S. Wise, Second-order convex splitting schemes for gradient flows with Ehrlich–Schwoebel type energy: application to thin film epitaxy, *SIAM J. Numer. Anal.* 50 (2012) 105–125.
- [20] C. Wang, X. Wang, S.M. Wise, Unconditionally stable schemes for equations of thin film epitaxy, *Discrete Contin. Dyn. Syst., Ser. A* 28 (2010) 405–423.
- [21] Y. Xia, Y. Xu, C.-W. Shu, Efficient time discretization for local discontinuous Galerkin methods, *Discrete Contin. Dyn. Syst., Ser. A* 8 (2007) 677–693.
- [22] Y. Xia, Y. Xu, C.-W. Shu, Local discontinuous Galerkin methods for the Cahn–Hilliard type equations, *J. Comput. Phys.* 227 (2007) 472–491.
- [23] C. Xu, T. Tang, Stability analysis of large time-stepping methods for epitaxial growth models, *SIAM J. Numer. Anal.* 44 (2006) 1759–1779.
- [24] Y. Xu, C.-W. Shu, Local discontinuous Galerkin methods for high-order time-dependent partial differential equations, *Commun. Comput. Phys.* 7 (2010) 1–46.